P505

Analysis and Prediction of a UV Laser Micro-machining Process

Wenwu Zhang, Y. Lawrence Yao and Kai Chen
Department of Mechanical Engineering
Columbia University, New York, NY 10027

Abstract

UV laser micro-machining of metallic materials has been used in microelectronic and other industries. Knowledge and data about the process vary with feature size, material, laser wavelength and pulse duration. This paper carries out experimental and numerical investigation of micro-machining of copper using a frequency tripled Nd:YAG laser with 50 nanosecond pulse duration. An axisymmetric model is developed and allows consideration of laser beam distribution and its coupling with the target material. This is important for the process where the removal extent is in the same order of the removal depth. The model uses enthalpy method to track the solid/liquid interface, Stefan and kinetic boundary conditions are applied at the liquid-vapor interface, and property discontinuity across the Knudsen layer is considered. Relevant experimental results are also presented and compared with the model predicted results. The range of thermal vaporization dominated machining of copper using nanosecond time scale lasers was studied, and optimum laser intensity for micro-machining of copper was suggested.

1. Introduction

Laser micro-machining is an established method for production of high precision features, especially in the microelectronic industry, such as via formation. The quality and profile of drilled holes have drawn increasing attention because of the increasingly reduced level of size and higher level of integration. UV lasers have been widely used for this purpose due to their better absorption. Using the Q-Switch techniques, they offer short pulse duration and high peak power, which limits heat affected zone and makes the material removal process dominated by ablation. Excimer lasers and frequency-tripled Nd:YAG lasers are among the most popular. Although copper is an important material in many applications, detailed study on laser machining of copper at micron level is not readily available.

Experimental work were done to investigate the laser ablation processes in order to understand the physics of laser material interactions. The process of thin Cu film removal at wavelength of 532 nm was studied (Hayashi and Miyamoto, 1995) and the effects of laser intensity on ablation mechanism was revealed. Thin film selective multishot ablation at 248 nm was also investigated (Hunger, et al., 1991). A systematic review of experimental results involving UV lasers can be found in Duley (1996). Many models of laser drilling have also been developed. Paek developed a theoretical model to predict the temperature profile assuming a laser beam of circular cross section and uniform intensity (Paek and Gagliano, 1972). Dabby calculated the transient temperature and penetrating velocity during the vaporization process (Dabby and Paek, 1972). The models more recently developed (Ho, et al., 1995; Kar and Mazumder, 1994) considered effects of gas dynamics and Knudsen layer discontinuity during the ablation process. These models assume 1D heat transfer in target material, recognizing that the machining depth is much smaller

than the diameter of the hole, which is reasonable for relatively large holes (a few hundred microns). As a result, however, the effects of beam profiles and cavity profiles are not considered. These factors are important when the size of the hole is comparable to the drilling depth. Modest developed a transient three-dimensional heat conduction model for material volume being machined (Modest, 1996). However, the model assumes that vaporization occurs in a single step without melting. Gas dynamics and discontinuity layer were not taken into account. This is not suitable for laser machining of metals on nanosecond time scale. Other models have been developed to study the phenomena of vapor plume and plasma during laser-plasma-solid interactions (Aden, et al., 1992; Singh and Narayan, 1990), some of which were developed with the application of thin-film deposition via laser ablation in mind.

The model in this paper concentrates on heat transfer and associated phase changes inside the target material, which is of major concern in machining applications. Stefan and kinetic boundary conditions are applied at the liquid-vapor interface, and property discontinuity across the Knudsen layer is considered. Heat conduction is calculated using enthalpy method. Most importantly, the axisymmetric model allows considerations of laser beam distribution and its coupling with the target material, which is important when the ablation extent is in the same order as the ablation depth. The model is capable of simulating the formation of cavity under the irradiation of pulsed UV laser beams with laser intensities less than 5×10^9 W/cm^2. Relevant experiments were also carried out.

2. Modeling background

Under the irradiation of a laser beam, target material is first heated from room temperature to melting temperature at which point melting takes place. Depending on laser intensity and material properties, the molten part of material will be evaporated by additional heating when it reaches the vaporization point and a vapor-filled cavity is formed (Fig. 1). A thin, so-called Knudsen layer exists at the melt-vapor interface, where the state variables undergo discontinuous changes across the layer (Knight, 1979). When the incident laser intensity exceeds a certain threshold, vaporization leads to plasma formation, which will absorb a certain percentage of laser energy. The more the intensity goes beyond the threshold, the denser the plasma, and the more percentage of absorption. In practice, an assisting gas jet could disperse the plasma plume sideward and lower the plasma density. But the plasma effects still exist. By introducing a correction coefficient in the modeling of laser intensity, the plasma effects are corrected for. The motion of molten material caused by Marangoni Effect (Bennett, et al., 1997) is neglected.

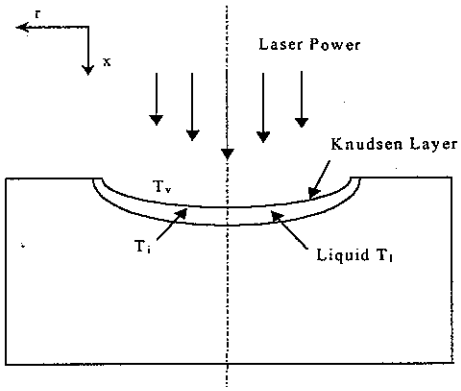

Fig. 1 Calculation domain

The governing equation for energy balance can be written as

$$\frac{\partial h}{\partial t}+\frac{\partial \Delta H}{\partial t}=\frac{\partial}{\partial x}(\alpha\frac{\partial h}{\partial x})+\frac{1}{r}\frac{\partial}{\partial r}(r\alpha\frac{\partial h}{\partial r}) \qquad (1)$$

where α is heat diffusivity and ρ is density, x and r are distances along axial and radial directions as shown in Fig. 1. The enthalpy of the material (the total heat content) can be expressed

as $H = h + \Delta H$, i.e., the sum of sensible heat, $h = c_p T$ (c_p is the heat capacity, and T is the temperature), and latent heat ΔH. It either varies with L_m, the latent heat for melting, or is zero. The enthalpy formulation allows one to trace the melting boundary as functions of time without regeneration of calculation grids (Voller and Prakash, 1987).

At the melt-vapor front, the Stefan boundary condition is applied,

$$Q + k(\frac{\partial T}{\partial x} + r\frac{\partial T}{\partial r}) + \rho_l v_i L_v - \rho_v v_v (c_p T_i + E_v) = 0,$$

$$E_v = \frac{RT_v}{(\gamma - 1)M_v} + \frac{1}{2}v_v^2,$$

$$Q = C(1 - Rl)I(t)e^{-(\frac{r}{b})^2} e^{-\beta x} \qquad (2)$$

where Q is the laser heat flux which depends on reflectivity Rl, absorptivity β and the plasma correction coefficient C. I is the laser intensity which is a function of time, and b is the laser beam radius. The subscripts l, v and i denote liquid phase, vapor phase and vapor-liquid interface, respectively. The gas energy E_v includes the internal energy and the kinetic energy. k is the heat conductivity, v the velocity, R the universal gas constant, γ the specific heat ratio, L_v the latent heat of vaporization, and M_v the molecular mass. The velocity, the laser energy flux and the heat conduction flux are valued along the normal direction of the cavity profile. The vapor-liquid front is determined by tracing the temperature. As long as the temperature at certain grid points reach vaporization temperature, the grids which have temperatures larger than vaporization temperature are taken out as the gas phase and the calculation starts from the newly determined vapor-liquid front.

A photo diode sensor is used to record the actual temporal distribution of the laser intensity. In simulation $I(t)$ takes the interpolated values at the current time. The plasma correction coefficient C is decided as follows.

$$C = 1 \qquad \text{if } I(t) < I_c,$$

$$C = 0.62927 - 0.5\tanh\frac{I - 2.4(I_{strong} - I_c)}{2.4(I_{strong} - I_c)} \qquad \text{if } I_c \le I(t) < 1.8 \times I_{strong},$$

$$C = 0.7118 \qquad \text{if } I(t) \ge 1.8 \times I_{strong} \qquad (3)$$

where I_c is the critical plasma generation value and I_{strong} is the strong plasma generation value. For copper at 355 nm, I_c=5×10^8 W/cm^2, I_{strong}=5×10^9 W/cm^2, then C = 0.87 at $I = I_{strong}$.

The reflectivity for UV wavelengths is

$$Rl = \frac{(n-1)^2 + k^2}{(n+1)^2 + k^2} \qquad (4)$$

where n is the index of refraction and k the extinction coefficient. For pure copper at wavelength $\lambda = 0.355\,\mu$m, n=1.34 and k=1.93, the absorption coefficient is given by

$$\beta = \frac{4\pi k}{\lambda} \qquad (5)$$

The following analytic relationships (Knight, 1979) are applied to account for the discontinuity of Knudsen layer.

$$\frac{T_{vi}}{T_{li}} = \left[\sqrt{1+\pi(\frac{m}{2}\frac{\gamma-1}{\gamma+1})^2} - \sqrt{\pi}\frac{m}{2}\frac{\gamma-1}{\gamma+1}\right]^2,$$

$$\frac{\rho_{vi}}{\rho_{li}} = \sqrt{\frac{T_{li}}{T_{vi}}}\left[(m^2+\frac{1}{2})e^{m^2}erfc(m) - \frac{m}{\sqrt{\pi}}\right] + \frac{1}{2}\frac{T_{li}}{T_{vi}}\left[1-\sqrt{\pi}me^{m^2}erfc(m)\right],$$

$$e^{m^2}erfc(m) \approx 0.34802a - 0.09588a^2 + 0.74786a^3,$$

$$a = 1/(1+0.47047m), m = \frac{v_{vi}}{\sqrt{2RT_{vi}/Ma_v}} \quad (6)$$

where subscript *vi* denotes the values of the vapor adjacent to the Knudsen layer and *li* the values of liquid adjacent to the Knudsen layer. Ma_v is the vapor Mach number, and *erfc(m)* the complementary error function.

The gas velocity is obtained from mass conservation:

$$\rho_l v_i = \rho_v(v_i + v_v), \quad (7)$$

where v_i is the velocity of melt-vapor interface and v_v is the vapor velocity.

The boundary conditions given by Eq. (2) depend on the vapor temperature, which is back related to vapor-liquid interface temperature through Eq. (6). Some thermal properties of copper are treated as temperature sensitive. The calculation process is thus iterative between the gas, liquid and solid phase until proper convergence is achieved. The properties used in simulation are listed in Appendix.

A control-volume based computation scheme was developed to solve the coupled governing equations. The two-dimensional discrete equations are written in the fully implicit form. The coefficients of variables are linearized between each time step to facilitate the convergence. The computational domain is taken large enough (5 times of beam radius in both x and r directions) so that the temperatures at external boundaries can be considered as room temperature. The convective and radiative heat transfer on the top surface is negligible compared with conduction heat loss and thus is not considered.

3. Experimental setup and beam property analysis

A Q-switched Nd:YAG laser with its fundamental frequency tripled (λ = 355 nm) and 50 nanosecond pulse duration was used as the UV energy source for experiments. The laser micromachining system includes UV laser source, polarizer, beam collimator, optical focus systems, CCD camera, TV monitor, micrometer table, and control software. Polarizer is used to adjust the laser intensity without affecting the stable operation of laser source and beam collimator is used to parallel and expand the beam for minimum focused spot size. A photon diode sensor is used to monitor the output laser pulses in real time. Copper foils with 99.9% purity and 0.3 mm thickness were polished before laser machining.

The focused laser beam size is required for laser intensity computation. But it is usually difficult to directly measure the focused beam, especially for cases when the focused spot size is below 10 microns. Experimental measurements were combined with optical calculations to overcome this difficulty. The spot size out of the collimator, which is several millimeters, was measured. For such dimension and intensity, knife-edge method was readily applied. Three measurements at different distances from the collimator were taken to obtain (Z_n, D_n), n = 1, 2, 3, where

D_n is the beam size at location Z_n. The laser beams satisfy the following equation (Orazio, 1998 and Steen, 1994):

$$D_n^2 = D_0^2 + (\frac{4M^2\lambda}{\pi})^2 \frac{(Z_n - Z_0)^2}{D_0^2}, \quad n = 1, 2, 3, \tag{8}$$

where D_0 is the beam waist, Z_0 is the beam waist location, and M^2 is the beam quality parameter to be determined. Knowing M^2, one can quickly calculate the beam divergence, focused spot size and depth of focus (*DOF*). For the laser used, it was found that $M^2 = 1.497$, minimum beam size $Dmin = 4.558$ μm, divergence at large distance $\theta_{infinity} = 44.96$ μrad, and $DOF = \pm 9.822$ μm.

4. Results and discussions

The computation domain of simulation is five times of the beam radius in both x direction and r direction. Uneven grids are used with denser grids near the center and the top, and the number of grids is 120×120. The laser beam intensity has a Gaussian distribution with $1/e^2$ beam radius b = 2.25 μm. The time step is 10 ns and the temperature field is considered converged when the relative error is less than 10^{-5}. From the simulation, cavity geometry, temperature distribution and melting surface recessing speed are predicted.

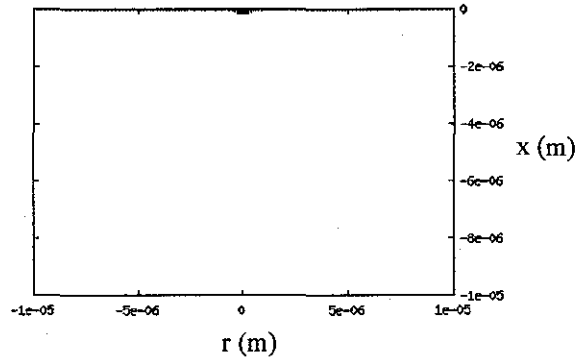

(a) I=4×10^7 W/cm^2

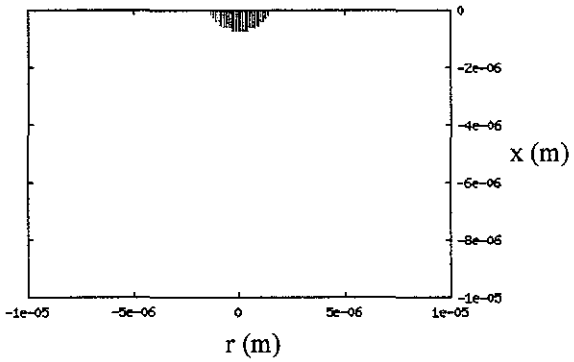

(b) I=8×10^7 W/cm^2

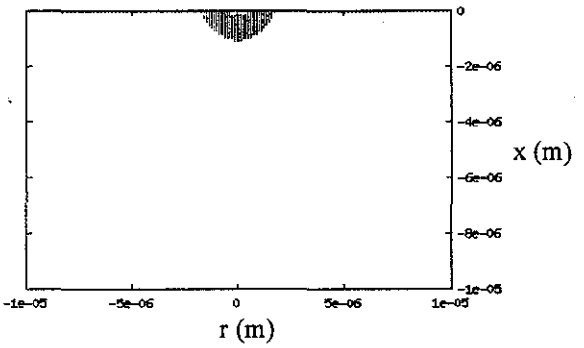

(c) I=1.15×10^8 W/cm^2

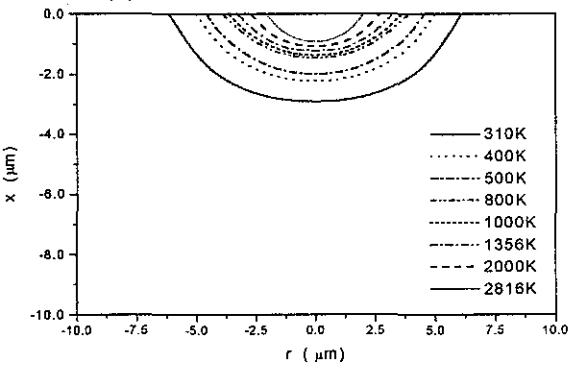

(d) Temperature contour at I = 6×10^8 W/cm^2

Fig. 2 Cavity profiles at the end of a 50 ns laser pulse (a) $I = 4\times10^7$ W/cm^2, (b) $I = 8\times10^7$ W/cm^2, (c) $I = 1.15\times10^8$ W/cm^2; and (d) Temperature contour at $I = 6\times10^8$ W/cm^2 (Wavelength λ = 355 nm, Gaussian beam, beam radius b= 2.25 μm, Cu. Vertical lines denote molten layer)

Fig. 2 a, b and c show the simulation results of the cavity profiles at the end of a 50-ns pulse at different levels of beam intensities. The material starts melting at 4×10^7 W/cm^2 (Fig. 2a). The material starts vaporization at 9.8×10^7 W/cm^2 and at 1.15×10^8 W/cm^2 a cavity on top is visible (Fig. 2c). In between pure melting evolves (Fig. 2b). The vertical lines denote the molten layer. Fig. 2d shows the temperature contours in the material after 50 ns for the intensity of 6×10^8 W/cm^2. It is seen that the temperature quickly drops to room temperature about three times of beam radius away from the cavity center with larger gradient close to the cavity surface.

Studying hole features at various laser intensities, it is found that melting is always present for metal ablation like copper at pulse duration of 50 ns. Only a very narrow range of intensity ($1.0\sim1.8\times10^8$ W/cm^2) was found to be dominated by vaporization. Outside of this range, molten metal motion develops gradually from nearly stationary at low energy levels ($I < 3\times10^8$ W/cm^2) to smooth flows at medium energy levels (3×10^8 W/cm^2 $< I < 8\times10^8$ W/cm^2) and to turbulent flows at high energy levels ($I > 8\times10^8$ W/cm^2).

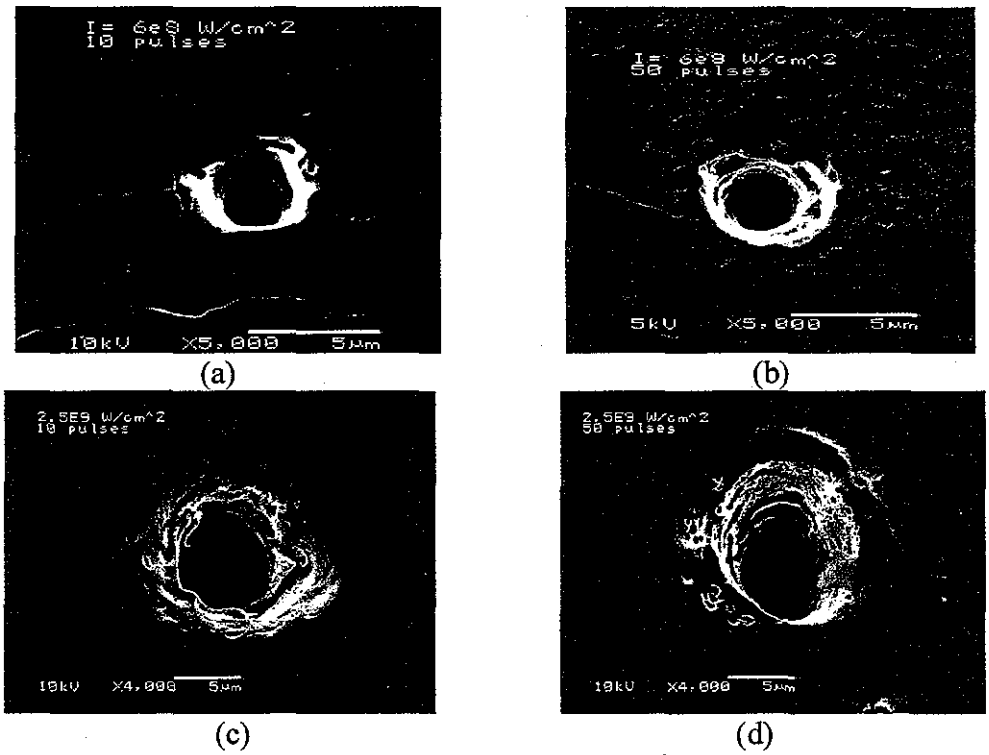

Fig. 3 SEM micrographs of laser drilled holes (a) $I = 6\times10^8$ W/cm^2, 10 pulses; (b) $I = 6\times10^8$ W/cm^2, 50 pulses; (c) $I = 2.5\times10^9$ W/cm^2, 10 pulses; and (d) $I = 2.5\times10^9$ W/cm^2, 50 pulses (Gaussian beam, beam radius $b = 2.25$ μm, pulse duration 50 ns, repetition rate 2 KHz, Cu)

Fig. 3 shows SEM micrographs of typical laser drilled holes. Fig. 3a and 3b are holes drilled at $I = 6\times10^8$ W/cm^2 using 10 pulses and 50 pulses, respectively. Fig. 3c and 3d are holes drilled at $I = 2.5\times10^9$ W/cm^2 using 10 pulses and 50 pulses, respectively. In both cases, samples were electropolished by about 0.15 μm for Fig. 3 a & b and 0.4 μm for Fig. 3 c & d. Holes drilled at 2.5×10^9 W/cm^2 show effects of stronger fluid motion than holes drilled at 6×10^8 W/cm^2. The recast layers of the holes are clearly seen. At 6×10^8 W/cm^2 the heat affected zones (HAZ) of the

holes are around 1 micron, while at 2.5×10^9 W/cm^2 the heat affected zones expand to more than three microns. The surface quality of the holes at 6×10^8 W/cm^2 is slightly better than that at 2.5×10^9 W/cm^2. The diameters of the holes changed from 3.3 μm at 6×10^8 W/cm^2 to 7.3 μm at 2.5×10^9 W/cm^2, while they remain almost the same for 10 pulses and 50 pulses at the same energy level. Thus choosing the suitable laser energy level is important for reducing drilling diameters and this diameter is relatively stable for pulse numbers larger than 10.

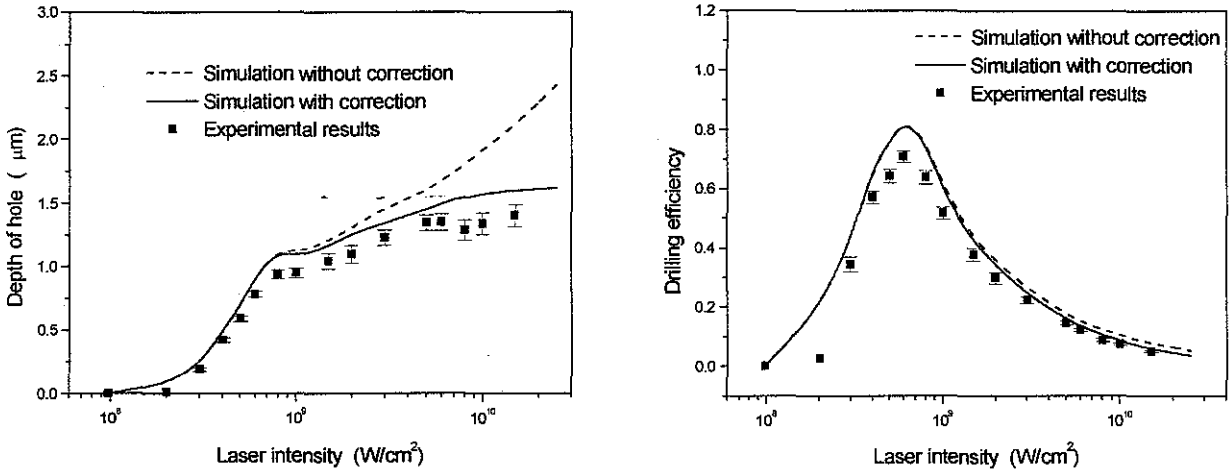

(a) (b)

Fig. 4 (a) Drilling depth per pulse; and (b) Drilling efficiency (Wavelength $\lambda = 355$ nm, Gaussian beam, beam radius $b = 2.25$ μm, pulse duration 50 ns, Cu)

Fig. 4a shows the relationship between the depth of hole and laser intensity. Both simulation and experiments show that although vaporization starts at $I > 0.98\times10^8$ W/cm^2, obvious vaporization starts at energy levels higher than 2×10^8 W/cm^2. Ablation depth per pulse increases with intensity, but at higher intensities ($I >$ 2e9 W/cm^2) the slope levels off. This is primarily due to plasma effects and part of the laser energy is absorbed and dissipated by the plasma. For laser intensity higher than 5×10^8 W/cm^2, plasma effect correction is necessary for the simulation model (Equation (3)). It is shown in Fig. 4a that simulation with correction agrees with the experimental data better than simulation without correction, especially when laser intensity is higher than 1×10^9 W/cm^2. Experimental drilling depth per pulse is lower than simulation results. This is likely due to the neglect of radiation heat losses. Another reason is that the experimental data is the average of multi-pulse drilling depth. The saturation of drilling depth for multi-pulses is shown in Fig. 6.

Fig. 4b shows how the drilling efficiency varies with laser intensity. Drilling efficiency is defined as (Duley, 1996)

$$\eta = \frac{[L_m + L_v + c_p(T_v - T_0)]X}{(1-Rl)I} \tag{9}$$

where T_0 is the initial temperature, X is the ablation depth per pulse, $(1-Rl)I$ is the absorbed laser energy. Peak efficiency of 0.837 is reached at 6.0×10^8 W/cm^2. Drilling efficiency is above 50% in the range of 3.35×10^8 W/cm^2 ~ 1.95×10^9 W/cm^2. Fig. 6b also shows that drilling efficiency with plasma effects correction agrees better with experimental data than those without correction.

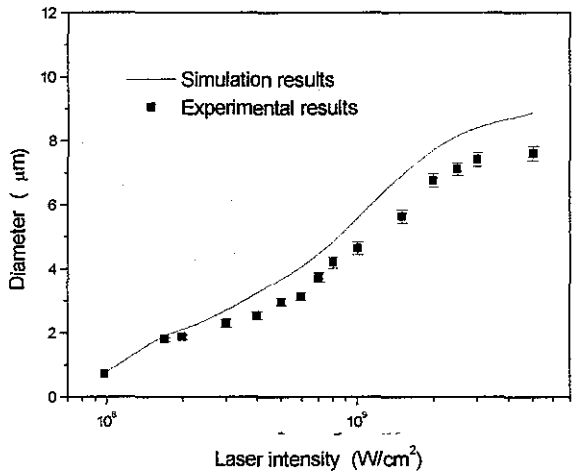

Fig. 5 Single pulse drilled hole diameters vs. laser intensity

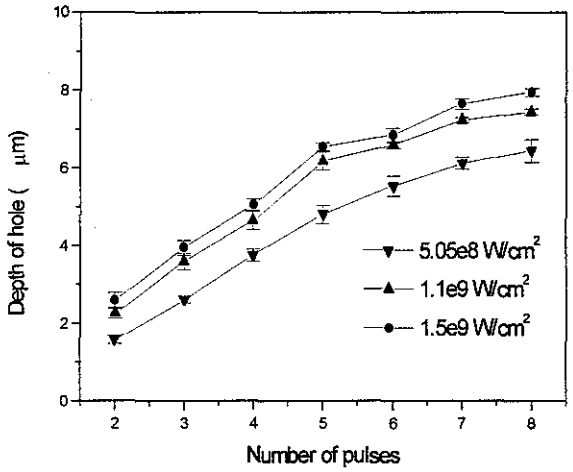

Fig. 6 Depth of holes at different energy levels vs. number of pulses (Beam radius 2.25 μm, pulse duration 50 ns, repetition rate 2KHz, Cu)

Fig. 5 shows how diameters of holes increase with laser intensities. Shrinkage in the cooling stage causes smaller holes than estimated values, so experimental diameters of holes are smaller than the simulation results. At intensities less than 1×10^9 W/cm^2 this difference is small and at higher intensities the diameters level off. This figure shows that below 5×10^9 W/cm^2 the fluid motion is relatively weak for the model to be effective. Beyond 5×10^9 W/cm^2 recoil pressure and strong fluid motion effects must be considered to give satisfactory predictions of the diameters of holes.

Fig. 6 shows the relationship between drilling depth and number of pulses at three energy levels. Depth of hole increases with the number of pulses, but after 5 pulses this increase deviates from the linear relation. The reason is that defocusing of laser beam and changes of cavity shape take effect. So real time focus control is necessary for precision deep-hole drilling. Fig. 7 shows the AFM analysis of a hole feature. The hole is drilled by two laser pulses at 6×10^8 W/cm^2. The profile is smooth and shallow, the depth is 1.681 μm and the diameter is 4.4 μm.

Fig. 8 shows the simulation results of the surface recess velocity distribution along the radial direction at $I = 6\times10^8$ W/cm^2. The velocity distribution clearly reflects the effect of Gaussian beam intensity distribution. The central velocity increases with time but saturates after 30 ns. It is obvious that the distribution at 10 ns and 20 ns have relatively flat distributions. The difference of the velocity distribution at different times is due to the change of cavity shape that alters the absorption of laser energy in the irradiated area. As time goes on, the central area absorbs more energy than the surrounding areas and the cavity becomes deeper and steeper. The recess velocities increase with time due to continuous energy accumulation within the pulse duration period, but the profile does not expand proportionally. Since the increase in central area is larger than that in other areas, the central area deepens faster than the surrounding area. This explains the tapering phenomena in laser drilling.

5. Concluding remarks

Physical aspects of UV laser micro-machining of copper are discussed. A numerical model to simulate the micro-scale cavity formation under a high-intensity, pulsed laser irradiation is pro-

vided. The simulation results of UV laser machining of copper at nanosecond and micron scales are presented and compared with experimental results. Drilling depth and hole diameter for a wide range of laser intensities are predicted for λ=355 nm and 50 ns pulse duration. Results show that melting of copper starts at around 6×10^7 W/cm^2, vaporization at around 1.06×10^8 W/cm^2, and obvious vaporization at 2×10^8 W/cm^2. Fluid flow is relatively weak below 1×10^9 W/cm^2 and plasma effects and gas dynamic effects should be considered at high intensities ($I > 5\times10^9$ W/cm^2). Only a very narrow range (1.06×10^8 to 1.8×10^8 W/cm^2) of vaporization dominated ablation exists for such nanosecond lasers.

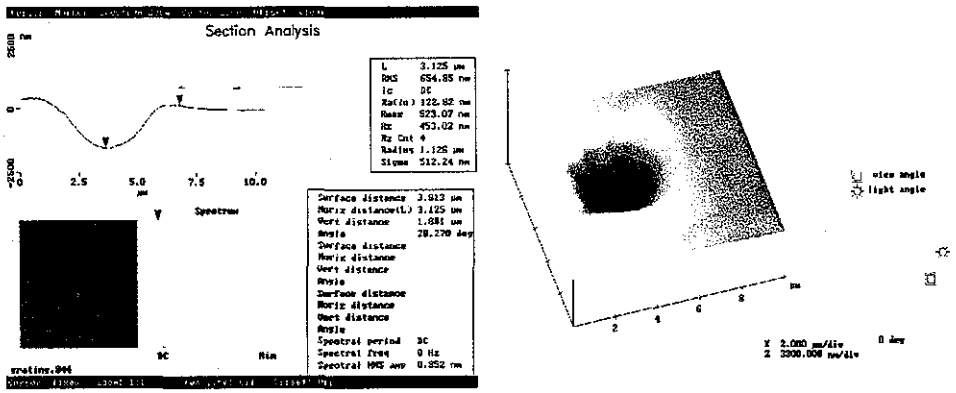

Fig. 7 AFM analysis of a hole drilled by 2 pulses at 6×10^8 W/cm^2 (Wavelength λ = 355 nm, Gaussian beam, beam radius b = 2.25 μm, Cu)

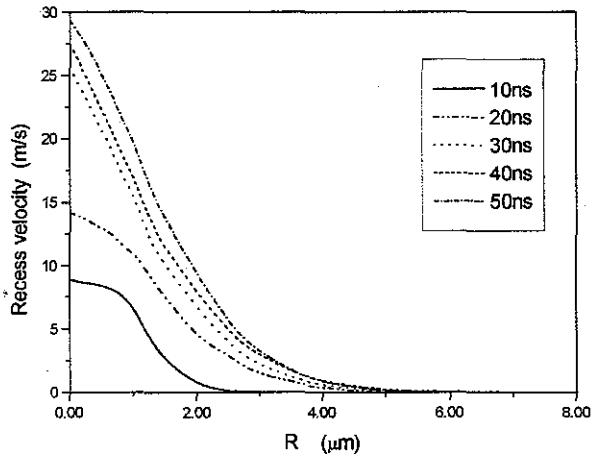

Fig. 8 Surface recess velocity at 6×10^8 W/cm^2 (Wavelength λ = 355 nm, Gaussian beam, beam radius b = 2.25 μm, pulse duration 50 ns, Cu)

6. Acknowledgements

Financial support from NSF under grant DMI-9813453 and equipment support from ESI are gratefully acknowledged. Assistance by Prof. Xuanhui Lu in setting up the experiments is also acknowledged. Assistance with AFM/SEM measurements and electropolishing rendered by Dr. Adrian Campbell, Dr. Alex Limanov and Dr. Yang Cao is appreciated.

7. Appendix

Properties of copper used in this paper: Density ρ = 8960 kg/m^3, melting temperature T_m = 1083°C, latent heat of melting L_m = 13.0 kJ/mol at 1atm, vaporization temperature T_v = 2543°C, and latent heat of vaporization L_v = 302 kJ/mol at 1atm. Other thermal properties of copper are treated as temperature sensitive and are interpolated from tabulated data in order to obtain reasonable calculation results (Grigoriev, et al., 1997). The isotropic specific heat capacity is given by $c_p(T) = 116.0 * \ln(T) - 31.8.27$. The

thermal conductivity for solid copper is
$k(T) = 406.375 - 0.02241 * T - 3.13091 \times 10^{-5} T^2 + 4.521 \times 10^{-9} T^3$, and for liquid copper
$k(T) = 27.892 + 0.17392 * T - 6.39142 \times 10^{-5} T^2 + 7.74766 \times 10^{-9} T^3$.

8. References

Aden, M., et al., 1992, "Laser-induced vaporization of a metal surface," *J. Phys.*, D 25, pp. 57-65.

Bennett, T.D., et al., 1997, "Marangoni Mechanism in Pulsed Laser Texturing of Magnetic disksubstrates," *J. Heat Transfer*, Vol. 119, pp. 589-596.

Dabby, F.W., and Paek, U.C., 1972, "High-intensity laser-induced vaporization and explosion of solid material," *IEEE J. of Quantum Electronics*, Vol. QE-8, No. 2, pp. 106-111.

Duley, W. W., 1996, UV lasers: effects and applications in material science, Cambridge, Cambridge University Press, 1996.

Grigoriev, I.S., and Meilikhov, E.Z., 1997, Handbook of Physical Quantities, New York, CRC Press, 1997.

Hayashi, H., and Miyamoto, I., 1995, "Process of thin Cu film removal by KrF Excimer laser," *ICALEO'95*, pp. 391-400.

Ho, J. R., et al., 1995, "Computational Model for the Heat Transfer and Gas Dynamics in the Pulsed Laser Evaporation of Metals," *J. Appl. Phys.*, Vol. 78(7), pp. 4696-4709.

Hunger, E., et al. 1991, "Thin film selective multishot ablation at 248 nm," *SPIE Lasers in Microelctronic Manufacturing*, Vol. 1598, pp. 19-26.

Kar, A., and Mazumder, 1994, "Mathematical model for laser ablation to generate nanoscale and submicometer-size particles," *J. Physical Review E*, Vol. 49(1), pp. 410-419.

Knight, C. J., 1979, "Theoretical modeling of rapid surface vaporization with back pressure," *AIAA Journal*, Vol. 17, No. 5, pp. 519-523.

Modest, M. F., 1996, "Three-dimensional, transient model for laser machining of ablating decomposing materials," *Int. J. Heat Mass Transfer*, Vol 39 (2), pp. 221-234.

Orazio Svelto, 1998, Principles of Lasers, 4th edition, New York, Plenum Press, 1998, pp. 148-158.

Paek, U. C., and Gagliano, F. P., 1972, "Thermal analysis of laser drilling processes," *IEEE J. of Quantum Electronics*, Vol. QE-8, pp. 112-119.

Singh, R. K., and Narayan, J., 1990, "Pulsed-laser evaporation technique for deposition of thin films: physics and theoretical model," *Phys. Rev. B* 41(3), pp.8843-8859.

Steen, W. M., 1994, Laser Material Processing, London, Spring-Verlag, 2nd Printing 1994, pp. 80-89.

Voller, V. R., and Prakash, C., 1987, "A fixed grid numerical modeling methodology for convection-diffusion mushy region phase-change problems," *Int. J. Heat Mass Transfer*, Vol. 30, No. 8, pp. 140-145.

Meet the authors

Wenwu Zhang is currently a Ph.D. candidate and Y. Lawrence Yao an Associate Professor in the Department of Mechanical Engineering at Columbia University, where Yao also directs the Manufacturing Engineering Program. Yao has a Ph.D. from Univ. of Wisconsin-Madison.